Pergamon

Int. J. Heat Mass Transfer. Vol. 39, No. 6, pp. 1183–1201, 1996

0017-9310/96 $15.00+0.00

0017-9310(95)00214-6

Numerical simulation of unsteady convective intrusions in a thermohaline stratification

J. WRIGHT and W. SHYY
Department of Aerospace Engineering, Mechanics and Engineering Science, University of Florida, Gainesville, FL 32611, U.S.A.

(*Received* 30 *November* 1994 *and in final form* 2 *June* 1995)

Abstract—The time-dependent development of convective intrusions in a thermohaline stratification is investigated using a composite grid method with local refinement. An imposed constant sidewall heat flux causes convective cells to form at the heated wall, which subsequently propagate into the bulk domain. For the composite grid computational method, a grid interface treatment based on strict local flux conservation alone allows arbitrary, nonphysical jumps in the temperature and salinity across block boundaries for certain boundary conditions. A revised treatment based upon a linear interpolation with conservative correction is employed to overcome this difficulty. Detailed features of the internal intrusion structure are captured and the sharp interfaces between neighboring intrusions are handled with fine resolution. Two classes of thermohaline intrusions corresponding to recently-obtained experimental results have been computed. Comparison with these results shows excellent agreement both qualitatively, in terms of the internal structure of the intrusions, and quantitatively, in terms of the physical size of the intrusions and the intrusion front propagation speeds. Fundamental differences in the merging processes for the two intrusion classes which were observed in the experiments have also been observed in the numerical results.

1. INTRODUCTION

Double-diffusive convection encompasses the spectrum of buoyancy-induced fluid motions which occur when two or more components having different molecular diffusivities and making opposite contributions to the fluid density gradients exist simultaneously. Since the molecular diffusivities of the components can often differ by an order of magnitude or more (such as when temperature and a salt are the two components of interest), the motions encountered in double-diffusive systems can be quite varied and complex, even for simple physical systems, as demonstrated by Bergman and Ungan [1], Kamakura and Ozoe [2], and Shyy [3] among others. The nature of double-diffusive flows and many reported findings can be found in the literature, including refs. [4–7]. Interest in this particular flow has stemmed primarily from observations of stably stratified convective layers in natural reservoirs, such as lakes and oceans [8, 9] as well as man-made systems, including solar ponds [10, 11].

The first experimental investigations of the lateral heating of a stably-stratified fluid were performed by Thorpe *et al.* [12] and Chen *et al.* [13]. Both studies considered a fluid of constant temperature with a vertical salinity gradient subjected to heating from a sidewall held at a fixed temperature above that of the initial temperature of the interior fluid. These investigations clarified the nature of the flow at the sidewall as an instability phenomenon by showing that under certain supercritical heating conditions, convection cells appear simultaneously along the entire heated portion of the wall. In addition, the nature of the formation and propagation of the intrusions was observed, where it was noted that the initial convection cells merged to form larger intrusions as they propagated laterally into the bulk of the domain. Chen *et al.* [13] proposed a vertical length scale for the initial intrusions, h, given by

$$h = \frac{\beta_T \Delta T}{\beta_S (\partial S/\partial y)_i} \qquad (1)$$

which characterizes the height to which a heated fluid element at the wall would rise in the initial density gradient. In the above expression, β_T represents the coefficient of thermal expansion, β_S represents the coefficient of expansion due to salinity, ΔT is the difference between the heated sidewall temperature and the initial temperature of the interior fluid, and $(\partial S/\partial y)_i$ is the initial vertical solute gradient, as designated by the subscript i. Based on this length scale, a critical Rayleigh number, defined by

$$Ra_c = \frac{g\beta_T \Delta T h^3}{\nu \alpha_T} \qquad (2)$$

of $1.5\times10^4 \pm 2.5\times10^3$ was established, below which lateral intrusions would not form. In equation (2), ν and α_T are, respectively, the kinematic viscosity and thermal diffusivity of the working fluid.

By performing a dimensional analysis of the governing equations and assuming that the length scales in

---

† Author to whom correspondence should be addressed.

NOMENCLATURE

B	source term due to buoyancy
g	gravitational acceleration
h	characteristic intrusion height
k	thermal conductivity
p	pressure
p^*	pressure due to fluid motion
P	Peclet number
Pr	Prandtl number
q	wall heat flux
Ra_c	critical Rayleigh number
R_l	lateral stability ratio
R_ρ	buoyancy ratio
S	solute concentration
S_0	reference solute concentration
Sc	Schmidt number
T	temperature
T_0	reference temperature
u, v	velocity components
x, y	horizontal and vertical coordinates.

Greek symbols

α_S	solutal diffusivity of fluid
α_T	thermal diffusivity of fluid
β_S	coefficient of solutal expansion
β_T	coefficient of thermal expansion
μ	dynamic viscosity
ν	kinematic viscosity of fluid
ρ_0	reference density.

both the horizontal and vertical directions are identical at initiation, Narusawa and Suzukawa [14] showed that in addition to the Prandtl number ($\Pi_1 = \nu/\alpha_\mathrm{T}$) and Lewis number ($\Pi_2 = \alpha_\mathrm{T}/\alpha_\mathrm{S}$, where α_S is the mass diffusivity of the solute), a third nondimensional parameter is given by the following:

$$\Pi_3 = \frac{-\beta_\mathrm{T}(q/k)}{\beta_\mathrm{S}(\partial S/\partial y)_i}, \qquad (3)$$

where q represents the constant applied lateral heat flux at the wall, k is the thermal conductivity of the fluid and the other quantities are as previously defined in equation (1). Since they considered a constant temperature fluid with only an initial linear solute stratification, this parameter can be physically interpreted as the ratio of the horizontal density gradient at the vertical heated sidewall to the initial vertical density gradient. For a constant sidewall heat flux, this third parameter was clearly identified as the appropriate stability parameter.

An experimental study of double-diffusive systems containing initial linear vertical stratifications of both temperature and salinity was recently carried out by Schladow *et al.* [15]. In their experiments, they used two nondimensional quantities to characterize the flows, one the Rayleigh (or buoyancy) ratio, given by

$$R_\rho = \frac{\beta_\mathrm{S}(\partial S/\partial y)_i}{\beta_\mathrm{T}(\partial T/\partial y)_i}, \qquad (4)$$

which is formed from the vertical saline and thermal Rayleigh numbers defined by the initial salinity and temperature gradients (again denoted by the subscript i), both of which are negative here, and the other a lateral ratio, defined by

$$R_\mathrm{l} = \frac{-\beta_\mathrm{T}(q/k)}{(-\beta_\mathrm{T}\,\partial T/\partial y+\beta_\mathrm{S}\,\partial S/\partial y)_i}. \qquad (5)$$

The Rayleigh ratio, R_ρ, provides a measure of the gravitational stability of the system, larger values indicating a higher gravitational stability. The lateral ratio, R_l, was proposed as a modification to the nondimensional parameter Π_3 used by Narusawa and Suzukawa [14] which explicitly takes into account the two-component vertical stratification. The quantity R_l provides a measure of the forcing at the heated sidewall and can also be interpreted as a ratio of the lateral density gradient at the sidewall to the initial vertical density gradient.

Three classes of intrusions, denoted as I, II and III, were clearly identified. Class I intrusions, which developed under conditions of relatively high gravitational and lateral stability ($R_\rho > 5$, $R_\mathrm{l} \approx 1$) were characterized by relatively quiescent, well-defined cells less than 10 mm thick. The internal structure of these intrusions consisted of a highly stable vertical temperature stratification and a well-mixed salinity field. The intrusions propagated at speeds less than 10 cm h^{-1} during the period in which the heat flux at the wall was applied and following removal of the heat flux, were observed to quickly diffuse away. Similar characteristics were observed by Narusawa and Suzukawa [14] for cases where the lateral stability parameter $\Pi_3 \leqslant 1$. In their case $R_\rho = \infty$ since they considered a constant temperature fluid. Intrusions categorized in class II developed under conditions of relatively low gravitational and lateral stability ($2.3 \lesssim R_\rho \lesssim 5$, $R_\mathrm{l} \gg 1$). These intrusions were observed to be larger ($\approx$10–40 mm thick), more dynamic, and less defined than class I intrusions. In contrast to class I intrusions, the vertical salinity stratification was found to be slightly unstable; however, the temperature field was still highly stable. In addition, intrusions categorized in class II propagated at much higher speeds ($\approx$10–30 cm h^{-1}) than class I intrusions. Like class I intrusions, they also diffused away immediately following removal of the sidewall heating. Class III intrusions developed under the conditions of lowest gravitational and lateral stability ($R_\rho \approx 2$, $R_\mathrm{l} \gg 1$) and were found to be the most dynamic of the three classes, propagating at speeds greater than 25 cm h^{-1}. While the physical appearances of class II and class III intrusions were observed to be very similar, the defining characteristic of class III intrusions was their ability to continue propagating long after the removal of the sidewall heating.

Regarding the intrusion merging process, it was noted that the physical mechanism for class I intrusions appears to be fundamentally different than that observed for classes II and III. Following the formation of the initial intrusions for a class I flow, merging seems to take place via a process whereby weaker intrusions are forced back to the heated wall by a blockage effect from the intrusions above and below, with no initial exchange of fluid between neighboring intrusions. Conversely, the merging process for class II and class III flows occurs via specific events, in which jets of fluid near the heated wall, originating from some intrusions, penetrate into neighboring intrusions from below, causing a breakdown of the interface separating the intrusions and leading to merger.

One of the first numerical simulations involving a stably stratified fluid subjected to lateral heating was performed by Wirtz and Liu [17]. They investigated the flow in a narrow slot with an initial linear solute stratification subjected to a constant temperature sidewall heating. Due to the lack of computational resources at the time, only extremely coarse grids could be used, and thus, no detailed analysis of the interaction between multiple convective cells could be considered. Other works have appeared in the literature since then, most notably those of Heinrich [18], Lee and Hyun [19] and Kamakura and Ozoe [2]. In each of these works, emphasis was placed on the basic qualitative details of the cell formation and the global features of the time-evolving flow field. The grid resolutions employed were also relatively coarse.

In this work, detailed numerical simulations of two of the experimental cases run by Schladow *et al.* [15] are performed with a composite grid method previously developed for Navier–Stokes flows. With a composite grid approach, the grid resolution considerations mentioned above due to the localized nature of the intrusion development can be handled very effectively. Within each block of the composite grid the SIMPLE algorithm [3, 20] is employed, whereby the momentum and continuity equations are solved in a sequential manner. The composite grid internal boundary treatment is based upon a locally, and thus globally, conservative treatment of the mass flux and tangential momentum flux through the boundary [21]. In the present context, as will be demonstrated later, an internal boundary treatment, in which the fluxes at the internal boundary are obtained entirely from the neighboring block in a locally conservative manner, allows an arbitrary jump in the temperature and salinity field across the interface which is non-physical for certain boundary conditions. To circumvent this problem, an interface scheme based upon a linear interpolation with conservative correction is employed, which allows the temperature and salinity fields to maintain the proper continuity conditions across the interface.

At the current time, it is still not feasible to simulate the flow in the entire experimental apparatus; however, this is not required. Although the overall physical sizes of the configurations computed here are smaller than the experimental apparatus (by a factor of two in the vertical direction, and a factor of 20 in the horizontal direction), the configurations are large enough to simulate flows with intrusion fronts composed of a sufficient number of convection cells in isolation from the influence of the physical boundaries, that direct comparisons with the experimental results can be made regarding keys points of interest including the intrusion front propagation speed, the internal characteristics of the intrusions (primarily temperature and salinity profiles), and details of the merging process.

2. GOVERNING EQUATIONS

The governing equations used here are the two-dimensional, time-dependent forms of the continuity, momentum, energy, and salinity equations obtained after employing the Boussinesq approximation. These can be written as

$$\frac{\partial u}{\partial x}+\frac{\partial v}{\partial y}=0 \tag{6}$$

$$\frac{\partial}{\partial t}(\rho_0 u)+\frac{\partial}{\partial x}(\rho_0 uu)+\frac{\partial}{\partial y}(\rho_0 uv) = -\frac{\partial p}{\partial x}+\frac{\partial}{\partial x}\left(\mu\frac{\partial u}{\partial x}\right)+\frac{\partial}{\partial y}\left(\mu\frac{\partial u}{\partial y}\right) \tag{7}$$

$$\frac{\partial}{\partial t}(\rho_0 v)+\frac{\partial}{\partial x}(\rho_0 uv)+\frac{\partial}{\partial y}(\rho_0 vv) = -\frac{\partial p}{\partial y}+\frac{\partial}{\partial x}\left(\mu\frac{\partial v}{\partial x}\right)+\frac{\partial}{\partial y}\left(\mu\frac{\partial v}{\partial y}\right)+B \tag{8}$$

$$\frac{\partial T}{\partial t}+\frac{\partial}{\partial x}(uT)+\frac{\partial}{\partial y}(vT)=\frac{\partial}{\partial x}\left(\alpha_{\mathrm{T}}\frac{\partial T}{\partial x}\right)+\frac{\partial}{\partial y}\left(\alpha_{\mathrm{T}}\frac{\partial T}{\partial y}\right) \tag{9}$$

$$\frac{\partial S}{\partial t}+\frac{\partial}{\partial x}(uS)+\frac{\partial}{\partial y}(vS)=\frac{\partial}{\partial x}\left(\alpha_{\mathrm{S}}\frac{\partial S}{\partial x}\right)+\frac{\partial}{\partial y}\left(\alpha_{\mathrm{S}}\frac{\partial S}{\partial y}\right) \tag{10}$$

where α_{T} is the thermal diffusivity, and α_{S} is the mass diffusivity of the salt. The term B in the vertical momentum equation, equation (8), is the source term due to buoyancy, and is expressed, using the Boussinesq approximation, by

$$B=\rho_0 g[\beta_{\mathrm{T}}(T-T_0)-\beta_{\mathrm{S}}(S-S_0)]. \tag{11}$$

The Boussinesq approximation assumes that the fluid density ρ, varies only slightly from a reference density state ρ_0, and can be expressed as

$$\rho = \rho_0 - \rho_0[\beta_T(T-T_0) - \beta_S(S-S_0)]. \quad (12)$$

In addition, the density variations are only assumed to produce the fluid motion via the source term B and are not considered to contribute to any of the other terms in the equations. For the cases considered here, variations in the density of less than 1% are expected, and so the assumptions made above are well satisfied. It should be noted that in the derivation of equation (8), the term $\rho_0 g$ was added and subtracted to obtain the given form of the source term. As a result of this, the pressure shown in the momentum equations explicitly contains the hydrostatic component, thus,

$$p = p^* + \rho_0 g y \quad (13)$$

where p^* represents the pressure in the Navier–Stokes equations which is due solely to the fluid motion. Discretization of the governing equations follows along the same lines as that detailed in Wright and Shyy [21], the only additions being the incorporation of the unsteady term in each equation and the buoyancy term in the v-momentum equation. In this work, we have adopted the use of the fully implicit scheme (Patankar [20]) for time marching, which is $\mathcal{O}(\Delta t)$ and central differences for the convection and diffusion terms.

3. COMPOSITE GRID METHOD

3.1. *Basics*

Since the continuity equation, equation (6), is identical to that previously used for isothermal, incompressible flows, and the momentum equations differ only by the presence of an additional source term, no changes are required to the original internal boundary treatment developed in Wright and Shyy [21]. The original conservation treatment developed there is based on the piecewise constant local conservation of the mass flux and tangential momentum flux through the internal boundaries, similar to that proposed by Rai [22]. For the pressure correction method, however, the mass and tangential momentum fluxes provide the required information for all boundary control volumes (continuity, u-momentum and v-momentum).

With the inclusion of conservation equations for temperature and salinity, an appropriate treatment for computing the temperature and salinity fluxes across the internal boundaries must be chosen. With a local conservation procedure, in which the flux boundary conditions for the temperature and salinity control volumes along the internal boundaries are computed entirely from the neighboring block, an arbitrary jump is allowed at the boundary for certain domain boundary conditions which cannot be detected. The possibility of this non-physical jump at an interface between blocks can be clearly seen from the multiblock solution of an equivalent one-dimensional model problem.

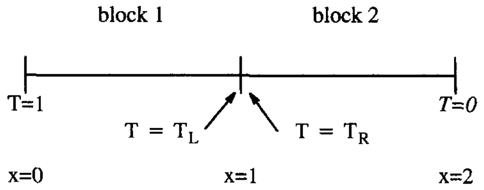

Fig. 1. Two-block domain for one-dimensional convection–diffusion equation, with temperature jump at interface.

Consider the solution of the convection–diffusion equation

$$P\frac{\partial T}{\partial x} = \frac{\partial^2 T}{\partial x^2} \quad (14)$$

on the two-block domain shown in Fig. 1, where P is the Peclet number. The left and right boundaries are held at fixed temperatures of 1 and 0, respectively, while the temperature at the center of the domain is taken to be T_L for the left block (block 1) and T_R for the right block (block 2), indicating a temperature jump of $\Delta T = T_L - T_R$. The exact solutions within the two blocks can be obtained as

$$T_1(x) = \left(\frac{T_L - 1}{e^P - 1}\right)e^{Px} + \left(\frac{e^P - T_L}{e^P - 1}\right) \quad (15a)$$

$$T_2(x) = \left(\frac{T_R\,e^{-P}}{1 - e^P}\right)e^{Px} + \left(\frac{T_R}{1 - e^{-P}}\right). \quad (15b)$$

Upon equalization of the total heat fluxes at the center of the domain, computed independently from each of the blocks, i.e.

$$\left(PT - \frac{\partial T}{\partial x}\right)_1\bigg|_{x=1} = \left(PT - \frac{\partial T}{\partial x}\right)_2\bigg|_{x=1} \quad (16)$$

the following relation is obtained

$$\left(\frac{1 - T_R}{T_L}\right) = e^{-P} \quad (17)$$

which states that the total fluxes can be balanced while still allowing a temperature jump $\Delta T = T_L - T_R$, which is a function of Peclet number and the values of either T_L or T_R. Thus, for an internal boundary treatment based on the local conservation of the total flux from the neighboring blocks, a temperature jump, the magnitude of which is dependent on the local flow conditions, is evidently permitted. For the isothermal flow cases considered previously in Wright and Shyy [21], mass flux conservation uniquely determines the normal velocity component at the interface. Since the normal and tangential velocity components at the interface are coupled through the continuity equation, no jump is permitted for the tangential velocity component from the solution of the tangential momentum equation, even though a locally conservative flux condition is employed.

In order to alleviate this temperature jump problem, an interface scheme based upon a linear interpolation procedure with a globally conservative correction has been implemented. By linearly interpolating within the neighboring block for the dependent variable (T or S) and using this value in conjunction with values in the block of interest to compute the total flux boundary condition, the proper continuity of the temperature and salinity fields can be maintained. The global correction is used to adjust the fluxes for each of the control volumes at the boundary so that the total temperature and salinity fluxes along the entire internal boundary separating the blocks are conserved. To illustrate the implementation procedure for this interface scheme, consider a typical temperature control volume at a vertical internal boundary, as shown in Fig. 2. With the original interface treatment, the temperature flux through the right control volume face is obtained using information exclusively from the neighboring block to the right via a local conservation procedure as detailed in Wright and Shyy [21]. Using this procedure, an arbitrary temperature jump cannot be detected since the gradient term $\partial T/\partial x$ is unaffected by a constant shift in the temperature field of the neighboring block. In order for the solution procedure to be able to detect the jump and adjust accordingly, the gradient term must be computed using information from the blocks on both sides of the boundary. Since the temperature at the control point on the left side of the interface, T_L, is already known, we must only obtain the temperature value T_L via linear interpolation from the neighboring block. With the specified boundary velocity value, u_B (already obtained from conservation of mass), the total heat flux through the right control volume face can be computed as

$$t\,\text{flux} = \left[0.5u_B(T_L+T_R)-\alpha_T\left(\frac{T_R-T_L}{\Delta x}\right)\right]. \quad (18)$$

Since this new procedure is no longer locally conservative, we can no longer expect global conservation to be automatically enforced, thus the need for a global correction. This is implemented by computing the total flux through line A independently from both blocks, using equation (18) for the fluxes out of the right block and then adjusting the temperature fluxes for each of the control volumes along the boundary by the required constant to obtain global conservation.

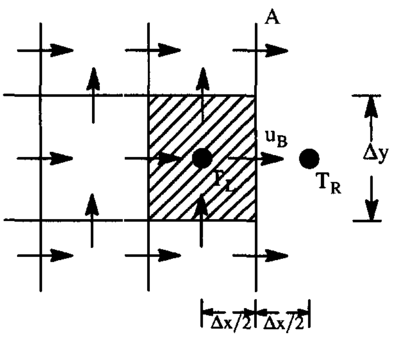

Fig. 2. Temperature control volume located at a vertical internal boundary.

In computing the fluxes for each temperature control volume along the interface, the use of linear interpolation is not essential, as any order of interpolation may be used for interpolating within the neighboring block (even piecewise constant). More importantly, whatever form of interpolation is used, the total flux (strictly only the diffusion term) must be computed using information from the blocks on both sides of the internal boundary in order to prevent temperature or salinity jumps from occurring. In this regard, it is important to note that if the endpoints of an internal boundary are not pinned through a Dirichlet boundary condition, then a locally conservative boundary treatment cannot be successfully applied (for the T and S equations) for multiblock problems requiring the solution of the temperature and/or salinity fields, since a locally conservative treatment by definition must compute the fluxes entirely from neighboring block information.

To compare the two interface treatments, the natural convection flow in a square cavity is computed. The boundary conditions for the flow and the grid are shown in Fig. 3i. The constant grid spacing in the horizontal direction is the same for both blocks, while in the vertical direction the grid spacing in block one is half that of block two. For this case, the overlap region consists of a single column of cells. The flow has been computed for a $Ra = 10^5$ based on the height of the cavity, and a $Pr = 0.71$. Figure 3iia,b shows the vertical temperature profiles in the overlap region near the center of the cavity for the solutions based on a local conservation treatment and the linear interpolation with correction treatment. It is clear that the locally conservative treatment of the total temperature flux is unsatisfactory, allowing a large temperature jump in certain regions, while the new treatment maintains the proper continuity along the entire interface. It is again important to note that at the upper and lower endpoints of the internal boundary, Neumann conditions on the temperature are prescribed. If Dirichlet conditions are prescribed on the upper and lower boundaries, then local conservation can be successfully applied to compute the temperature fluxes since a unique solution will be imposed to meet the fixed boundary constraints.

3.2. *Grid refinement strategy*

It is clear that a very fine grid resolution is required in the region near the intrusions, while a much coarser grid is sufficient away from the intrusions. A single grid, clustered in the region near the intrusions might be sufficient; however, due to the preferred directionality of the flow, in which a very fine vertical spacing must be used to capture the nearly horizontal interfaces between the intrusions, this choice is not optimal, since the fine vertical resolution in the near wall region will also be imposed on the far-field flow.

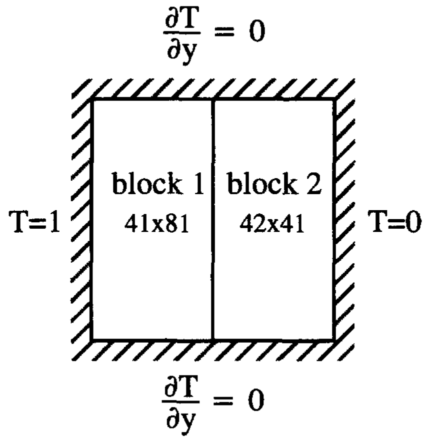

(i) Domain, boundary conditions and block resolutions.

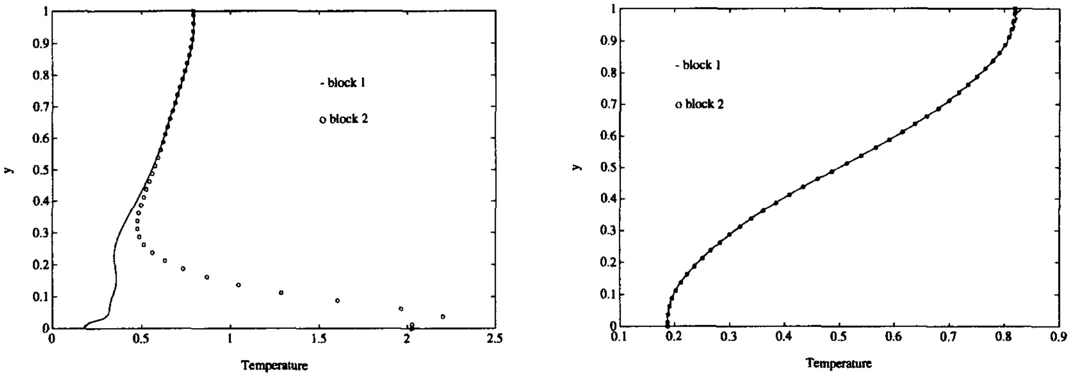

(a) (b)

(ii) Temperature profile along vertical centerline for different interface treatments. (a) Local flux conservation, (b) Linear interpolation with global flux correction.

Fig. 3. Grid layout, boundary conditions, and solutions of the two-block approach for natural convection in a square cavity.

In our simulations, a two-block composite grid is used to track the evolution of the sidewall intrusions. One block, with a very fine horizontal and vertical resolution is placed in the near-wall region, and a second block with a relatively coarse horizontal and vertical resolution is used in the bulk of the domain. As the intrusion front moves into the bulk fluid, grid lines are added to the fine grid and removed from the coarse grid, so that the fine-grid/coarse-grid interface remains ahead of the intrusion front. A visual representation of this grid refinement process for the development of class I-type intrusions is shown in Fig. 4. In the following section, we give a detailed presentation of the simulations which have been performed.

4. NUMERICAL SIMULATION RESULTS

4.1. *Basics*

Two numerical simulations were performed, one corresponding to the development of class I intrusions and the other to class II intrusions. For both simulations, a 20 cm high by 20 cm wide domain was used. In the experiments performed by Schladow *et al.* [15], the tank used was 50 cm high and 400 cm wide. This height is sufficient to accommodate approximately 30 class I intrusions and 10 class II intrusions along the heated left wall, based on the intrusion thickness after completion of the initial merging process, and taking into account the unstratified fluid layers employed at the top and bottom of the tank. Similarly, a domain

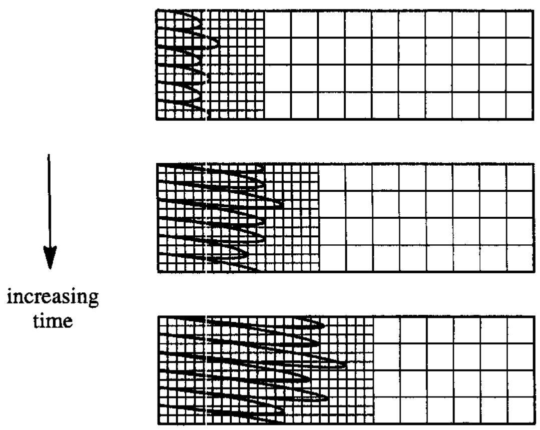

Fig. 4. Composite grid tracking of sidewall intrusions.

of 20 cm in height should allow approximately 10 class I intrusions and 5 class II intrusions to develop along the heated wall, which should be sufficient to allow comparison with the experimental results for the key points mentioned previously. Concerning the apparent disparity in the tank widths, it is noted that for the duration of the experiments, completely through the final merger process (with the exception of the self-propagation cases for class III flows), the intrusion fronts penetrated no more than about 25 cm into the tank, and thus, a large portion of the tank remained essentially quiescent, except for the small disturbances created by the presence of the intrusions.

The initial stratifications of temperature and salinity were prescribed as follows. At the top of the domain, a 3 cm unstratified zone was set, followed by a linear stratification region of 14 cm, and then another 3 cm unstratified zone at the bottom. In the experimental simulations, unstratified layers were also employed at the top and bottom of the tank to provide a nearly constant zero flux condition for temperature and salinity for the duration of the experiment. Since these flux conditions can be exactly enforced in the numerical simulations, the unstratified zones used here serve only as a buffer region, effectively isolating the intrusion front from the effects of the upper and lower walls. Figure 5a shows the domain used for the numerical simulations, the boundary conditions and the initially imposed temperature and salinity stratifications. The prescribed sidewall heating fluxes, specified initial temperature and salinity stratifications and the corresponding Rayleigh ratio, lateral stability ratio and intrusion classification for the numerical simulations are summarized in Table 1. These simulations correspond exactly (in terms of the values of R_p and R_l) to the two experimental cases reported in detail. As the mean stratification temperature and salinity of the NaCl-based solution at the start of the experimental simulations were unknown, the numerical simulations were assumed to occur at a starting mean stratification temperature of 20°C and a mean salinity stratification of 30 kg m^{-3}, for which the physical parameters of water, such as the kinematic viscosity, thermal diffusivity and mass diffusivity, all assumed constant, were taken from Akbarzadeh and Manins [10]. Thus, small differences in both the thermal and solutal Rayleigh numbers may exist between the experimental and numerical simulations for each case, although the Rayleigh ratios, R_p, and lateral stability ratios, R_l, are the same. With the fluid properties above,

$$Pr = \frac{\nu}{\alpha_T} = 8 \quad \text{and}\ Sc = \frac{\nu}{\alpha_S} = 675.$$

The grid used for the simulations, as mentioned previously, is composed of two blocks, a fine block in the vicinity of the heated wall and a coarse block away from the wall. In the initial grid, the fine block consists of 131×501 nodes, while the coarse block has 162×251 nodes. In the fine grid block, the grid lines have been clustered toward the heated wall, resulting in a grid spacing of $\Delta x = 0.012$ cm (0.06% of overall domain width) at the wall ($x = 0.0$) and increasing linearly to $\Delta x = 0.05$ cm at $x = 4.0$ cm. The vertical grid spacing in the fine block is uniform, with $\Delta y = 0.04$ cm. In the coarse block, the grid lines are uniformly spaced in both directions, resulting in grid spacings of $\Delta x = 0.1$ cm and $\Delta y = 0.08$ cm. Since the last two vertical columns of the fine grid have a grid spacing of $\Delta x = 0.05$ cm, the overlap region of the fine and coarse grids consists of exactly two fine grid cells and one coarse grid cell.

As the solution advances in time, the intrusion front will eventually approach the fine/coarse grid interface of the initial grid and re-meshing will be required. Re-meshing is carried out here when the fastest moving intrusion approaches a distance of about 1 cm from the interface. Since the intrusion fronts for class I and class II flows propagate at different speeds, the times at which re-meshing occurs will be different. When re-meshing is required, a 4.0 cm extension is added to the fine grid, while 4.0 cm of the coarse grid is removed, producing the new mesh. The grid spacings in the newly added portion of the fine mesh are taken to be uniform, with values of $\Delta x = 0.05$ cm and $\Delta y = 0.04$ cm. This process results in a new mesh composed of a fine block with 211×501 nodes and a coarse block with 122×251 nodes. Values for the solution at the newly introduced fine grid nodes are taken from the coarse block via linear interpolation before the coarse block is restructured. As the solutions progress, a second re-meshing may also be required, in which case a similar procedure as that described above for the first re-meshing is invoked. Figure 5b shows the sequence of grids employed in the simulations.

For both simulations, a time step $\Delta t = 0.2$ s was used. Since the maximum fluid velocities are $\mathcal{O}$(1 mm s^{-1}), this value was heuristically chosen so that between successive time steps, the fastest fluid particles will have traversed at most one grid cell. To verify this choice, a single-block grid simulation corresponding

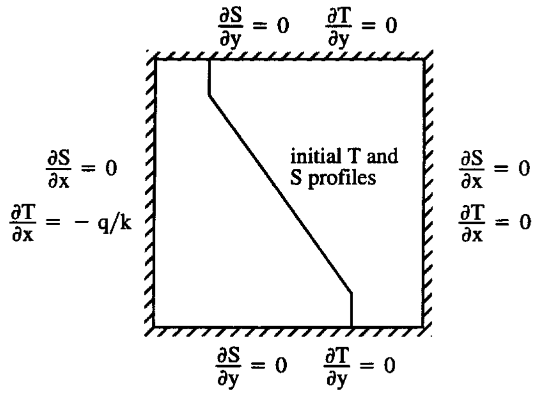

(a) Physical domain, boundary conditions, and initial T and S profiles for numerical simulations.

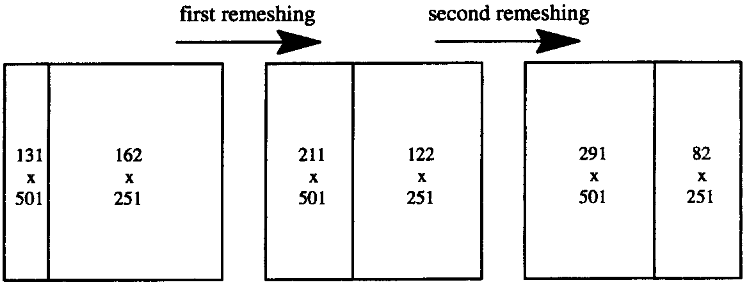

(b). Sequence of grids employed in numerical simulations.

Fig. 5. Boundary and initial conditions and grid structure of the present problem.

Table 1. Parameter specifications for numerical simulations

Intrusion class	Side wall heat flux ($W m^{-2}$)	Initial dT/dy ($K m^{-1}$)	Initial dS/dy ($kg m^{-4}$)	Rayleigh ratio R_p (equation 4)	Lateral ratio R_l (equation 5)
I	91.67	−25.37	−129.58	8.3	0.9
II	91.61	−7.01	−13.80	3.2	10.8

to the class I simulation described above was performed with time steps of $\Delta t = 0.1$ s and $\Delta t = 0.2$ s. The grid consisted of 301×301 uniformly spaced nodes. At a physical time of 2 min, vertical profiles of the field variables were taken at a location near the heated wall. Comparison of the profiles for the two time steps indicated that the solution appeared to be time-step independent near $\Delta t = 0.2$ s. In this regard, it is noted that the time step employed by Schladow *et al.* [15] in their numerical simulation, $\Delta t = 0.0125$ s, seems excessively small, since the minimum grid spacing used there was 0.03 cm, which is very close to that employed in the current numerical solutions. In the following, we first present results for the class I simulation, followed by results for the class II simulation.

4.2. *Results for class I simulation*

A sequence of contour plots showing the development of class I intrusions from the beginning of the numerical simulation to the termination time of 36 min is shown in Figs. 6–8. Contours of streamfunction, temperature and salinity have been plotted at each chosen time. In each of the contour plots, only the portion of the domain corresponding to the initial stratified region (3 cm $\leqslant y \leqslant$ 17 cm) has been included. The initial intrusions form along the heated wall at a time of about 10 min, and by about 28 min,

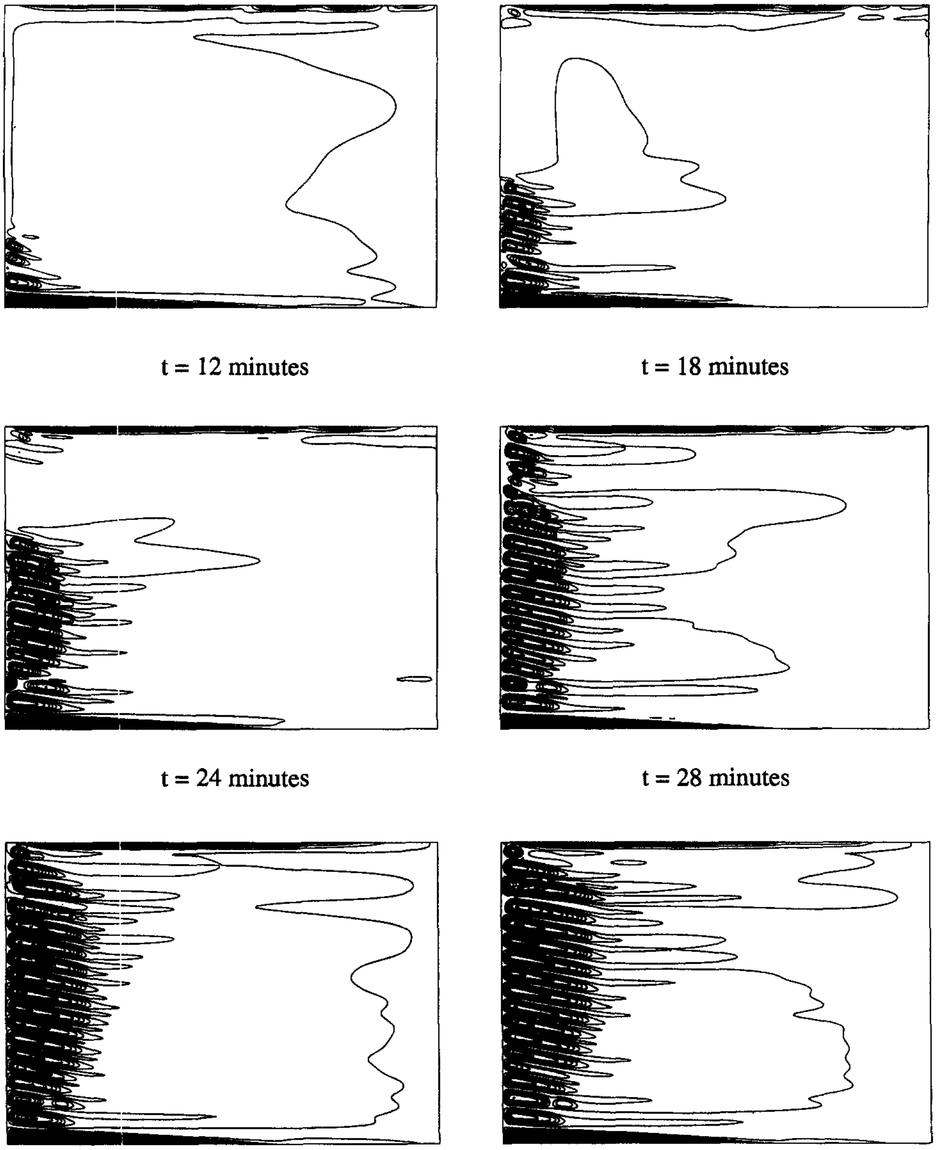

t = 12 minutes

t = 18 minutes

t = 24 minutes

t = 28 minutes

t = 32 minutes

t = 36 minutes

Fig. 6. Stream function at various times of class I intrusions.

have spanned the entire stratified region along the wall. In agreement with experiment, the intrusions form exclusively from the bottom of the domain to the top (with the exception of some small circulation regions near the top). The characteristic downward-sloping appearance of the intrusions, observed in all experiments for these flows, is also observed here. From the streamfunction plots, it is apparent that class I intrusions are characterized by relatively quiescent motions, producing a well-defined layered structure with distinct intrusions separated by thin, nearly-horizontal interfaces.

Vertical profiles of the temperature and salinity for the full domain height, taken at a distance of 3.0 cm from the heated wall (15% of width from wall), corresponding to the times shown in Figs. 6–8 are given in Figs. 9 and 10, respectively. The class I profiles are given here at a distance of 3.0 cm from the wall (unlike the profiles for the experimental results which are presented at 1.3 cm) to allow better comparison with the characteristics of class II profiles (later presented at 3.0 cm from the wall). From these plots, the step-like nature of the intrusions is clearly evident, where it is observed that that a stable temperature profile and a well-mixed salinity profile have developed in each of the intrusions. Both of these characteristics were observed in the corresponding experimental case for this class. The numerical results predict larger inversions than experiment, as can be seen by a comparison of Fig. 9 with Fig. 4 (in ref. [15]).

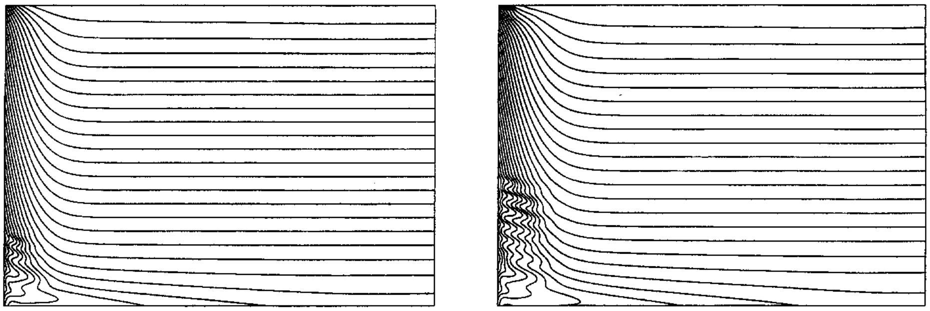

t = 12 minutes t = 18 minutes

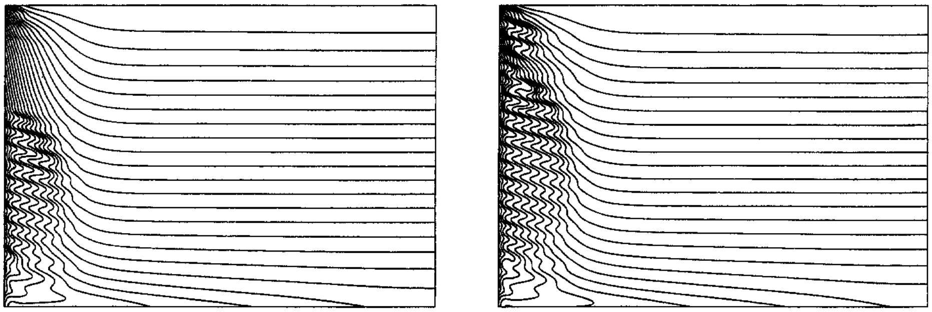

t = 24 minutes t = 28 minutes

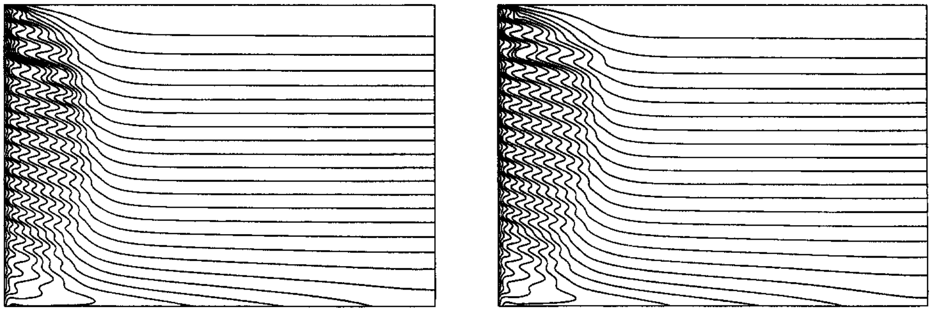

t = 32 minutes t = 36 minutes

Fig. 7. Isotherms at various times of class I intrusions.

It is unclear at this point whether this discrepancy is attributable to the numerical procedure or the experimental method for obtaining the vertical temperature profiles. For this particular flow, due to the small thickness of the intrusions, it is noted that the experimental results have quite a limited resolution. In addition, it is interesting to note that the numerical results performed by Schladow *et al.* [15] for a similar class I case (Fig. 9 in ref. [15]) also predict more pronounced temperature inversions than the experimental results.

Results for the overall size of the intrusions and the front propagation speed also show favorable agreement with the values observed experimentally. For the numerical simulation, the average height of the intrusions measured at the heated wall at a time of 36 min is approximately 8 mm. The corresponding experimental value, taken from photographic images at a similar time, is about 10 mm. Using the sequence of streamfunction contour plots shown in Fig. 6, the intrusion front speed is estimated to be approximately 7 cm h^{-1}. In this computation, only the 10 intrusions located about the center of the stratified region were used, since the development of the intrusions near the upper and lower portions may have been hindered by the fairly strong recirculation regions which exist in the unstratified layers at the top and bottom of the domain. In this regard, the attempt to isolate the intrusion front from the effects of the solid walls by including unstratified layers above and below, may

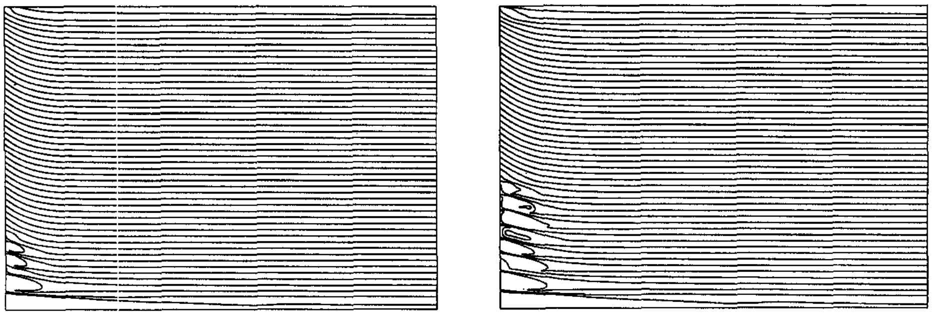

t = 12 minutes t = 18 minutes

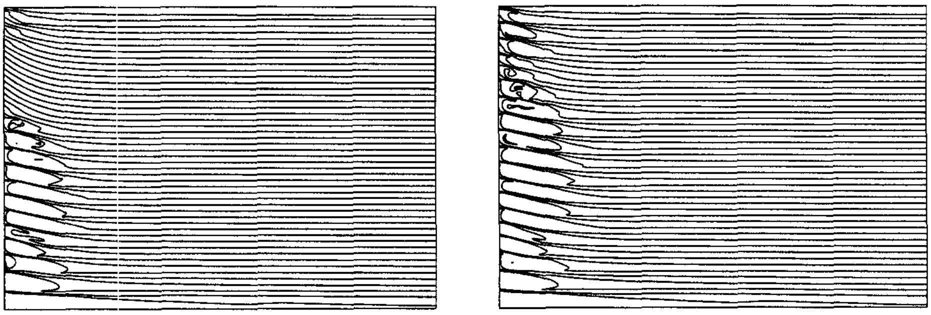

t = 24 minutes t = 28 minutes

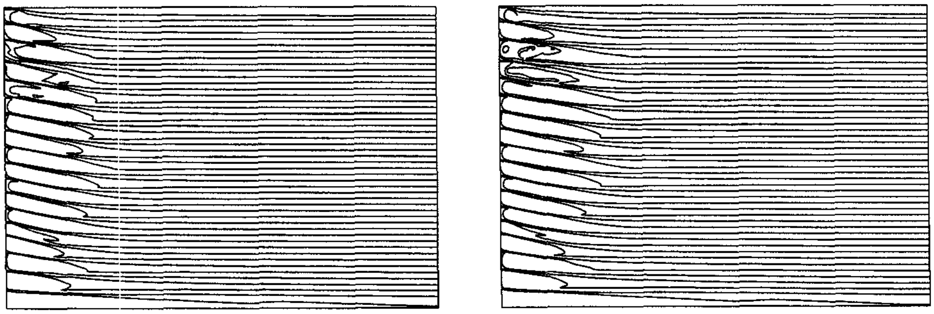

t = 32 minutes t = 36 minutes

Fig. 8. Salinity contours at various times of class I intrusions.

have resulted in a greater disturbance to the upper and lower intrusions than would have existed without these layers. No value for the average speed of the intrusions for the corresponding experimental case was given, but the value computed above does agree favorably with the speed of 10 cm h^{-1} or less which was generally observed for class I intrusions.

Regarding the merger process, some evidence of the blockage mechanism described earlier, and observed clearly in the experiments, can be seen in the final four frames of the streamfunction contour sequence shown in Fig. 6 for the fourth intrusion from the bottom. From a time of 24 min to 36 min, a progressive weakening of this intrusion is clearly evident as it becomes overtaken by its upper and lower neighbors. Consistent with the description of the merger mechanism, no exchange of fluid between neighboring intrusions appears to initiate the process of merger, since the interfaces between the intrusion and its upper and lower neighbors are clearly seen to be maintained during the entire process.

4.3. *Results for class II simulation*

A sequence of contour plots for the development of the class II intrusions in increments of 4 min from the beginning of the simulation to the termination time of 20 min is shown in Figs. 11–13. Again, only the portion of the domain corresponding to the initial strati-

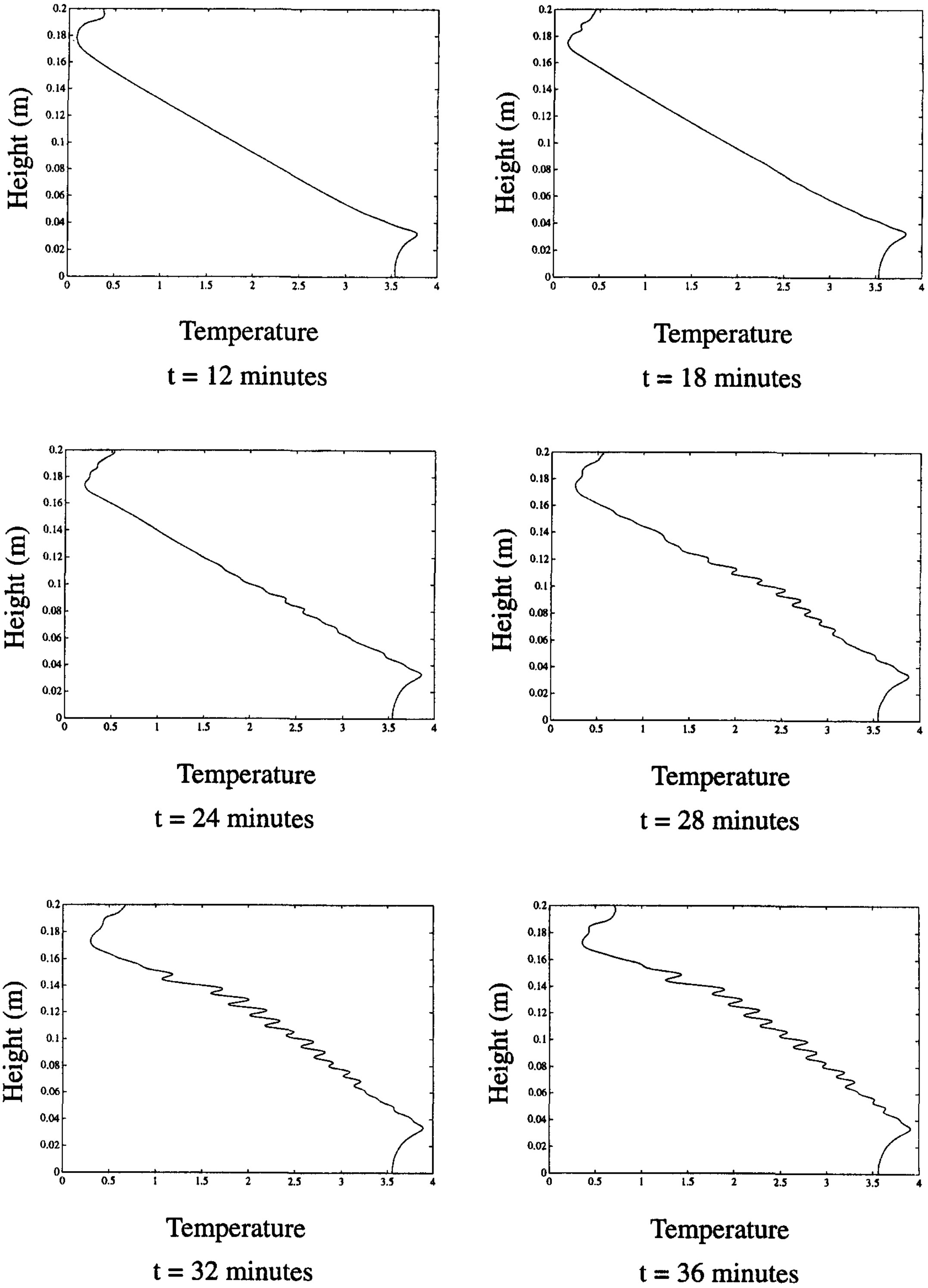

Fig. 9. Temperature profiles at 3.0 cm from the heated wall at various times (class I).

fied region has been included. The initial intrusions form along the heated wall at a time of about 2 min, eventually spanning the length of the heated wall in the stratified region by a time of 5 min. As time elapses, the characteristic structure of the flow becomes evident, where again, fairly well-mixed regions are separated by distinct interfaces in which sharp gradients of temperature and salinity exist. It is apparent from the salinity contours that class II intrusions are much more dynamic and contain a much finer salinity

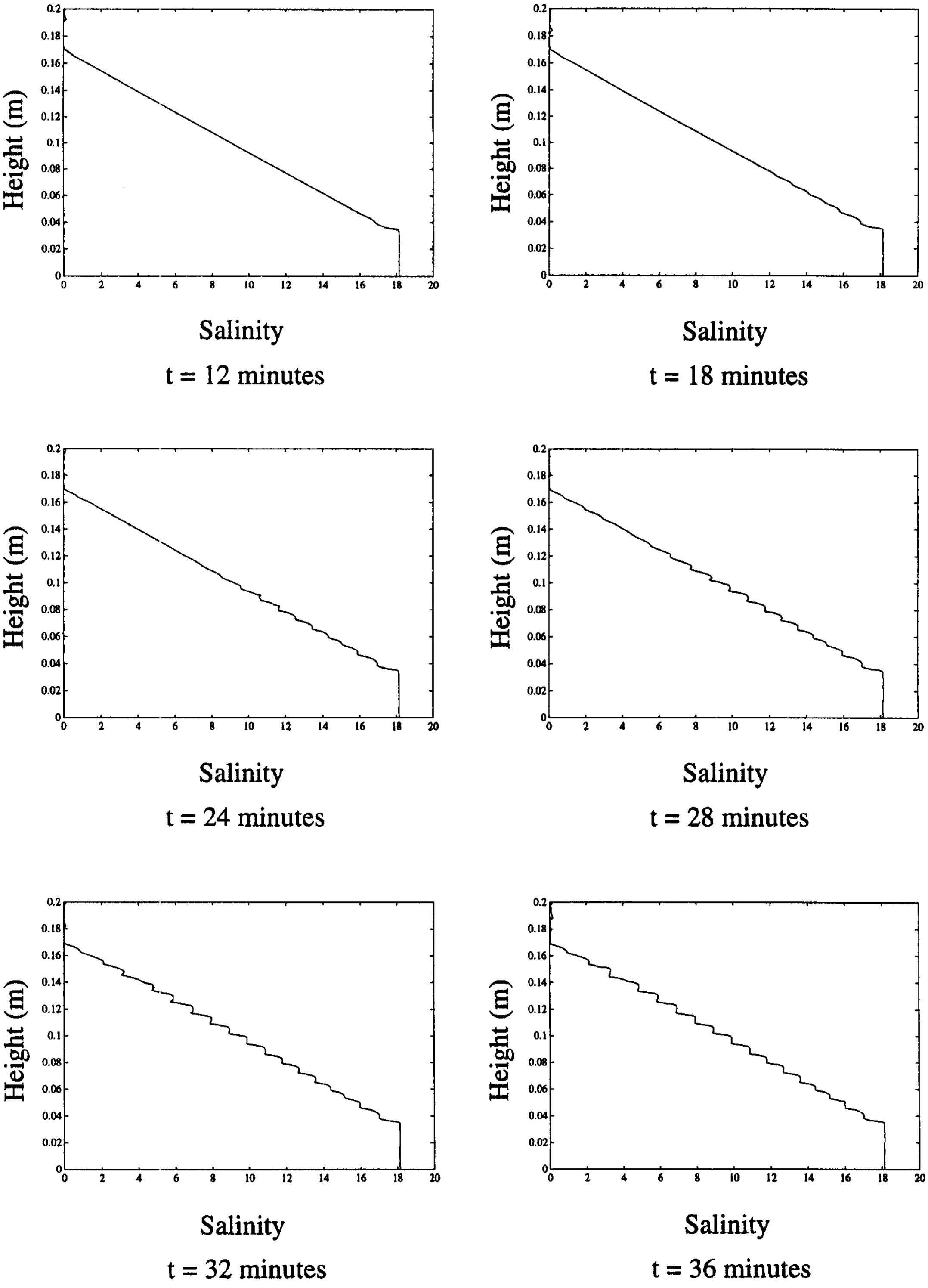

Fig. 10. Salinity profiles at 3.0 cm from the heated wall at various times (class I).

structure due to the highly convective nature of the flow within the intrusions.

Figures 14 and 15 display, respectively, vertical profiles of the temperature and salinity (again taken 3.0 cm from the heated wall) for the full domain height corresponding to the times shown in Figs. 11–13. It is again observed that a highly stable temperature profile has developed in each of the intrusions. In contrast to the class I intrusions, in which the salinity was well-mixed, the salinity distribution in the class II

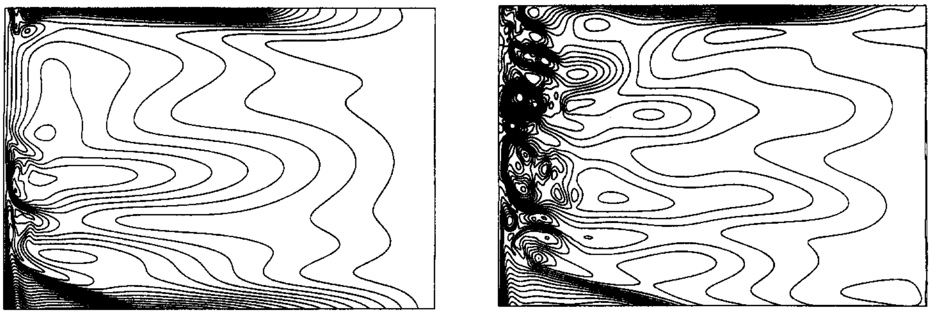

t = 4 minutes t = 8 minutes

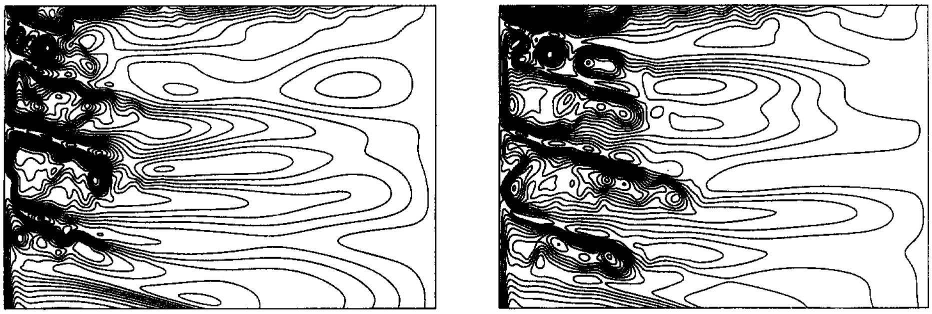

t = 12 minutes t = 16 minutes

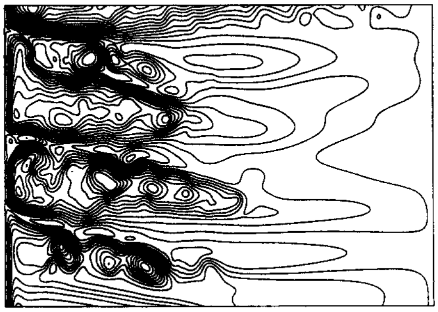

t = 20 minutes

Fig. 11. Stream function at various times of class II intrusions.

intrusions is observed to be slightly unstable. These characteristics for the internal temperature and salinity profiles were also observed in the corresponding experimental case. In contrast to the class I case, the temperature inversions within the intrusions compare more favorably with experiment. The slope of the temperature profile (which is nearly constant) within the middle intrusion, as computed from Fig. 5 in ref. [15] is about 0.11°C cm^{-1}, while that computed for the middle intrusion from Fig. 14 at $t = 20$ min is about 0.14°C cm^{-1}. Regarding the apparent "jagged" behavior of the salinity profiles compared to the temperature profiles, it is noted that since the Schmidt number is very large ($Sc = 675$), the fine scale salinity structure of the intrusions is essentially being convected with diffusion contributing only within small length scales. A comparison of the salinity profiles in Fig. 15 with those in Fig. 5 (in ref. [15]) shows that the numerical simulation predicts a more highly fluctuating salinity distribution throughout the intrusion interiors. These small-scale fluctuations are probably not evidenced in the experimental profiles since the raw experimental data was passed through a low-pass filter before plotting.

Results for the overall size and front propagation speed again show favorable agreement with the values observed for typical class II intrusions. Based on the general observations of the experiments, the final height for typical class II intrusions was found to fall in the range 10–40 mm. From the salinity and

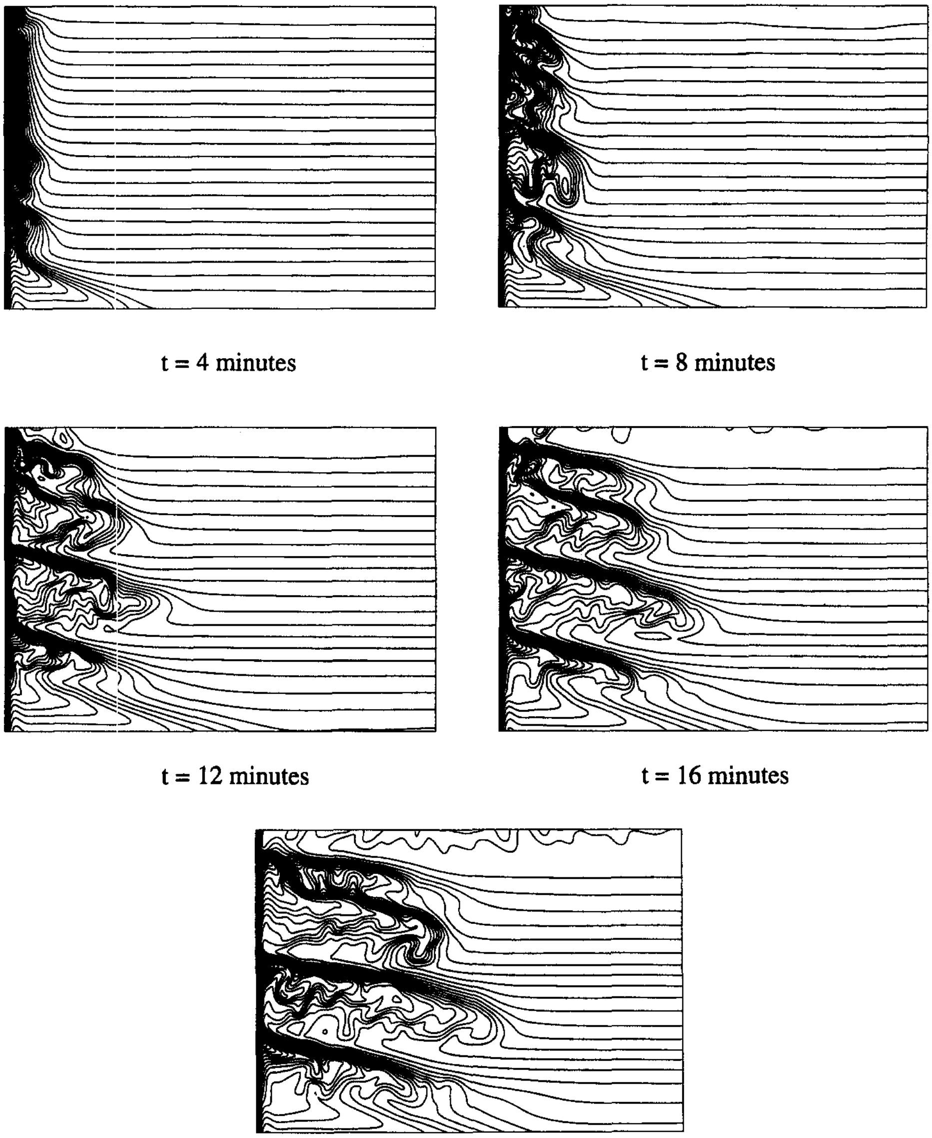

t = 4 minutes

t = 8 minutes

t = 12 minutes

t = 16 minutes

t = 20 minutes

Fig. 12. Isotherms at various times of class II intrusions.

temperature profile plots for the experimental case corresponding to the current numerical simulation, taken 3 cm from the heated wall at a time of 19 min, the average height of the intrusions is estimated to be about 40 mm. Based on a similar analysis of the temperature and salinity profiles for the numerical simulation, an average intrusion height of about 35 mm is obtained. Using the salinity contour sequence shown in Fig. 13, the intrusion front speed was computed to be about 27 cm h^{-1}. In this computation, only the two center intrusions were used. This value also agrees very well with the range of 10–30 cm h^{-1} observed in the experiments for class II flows. Again, no estimate of the front propagation speed for the specific experimental case corresponding to the numerical simulation was given.

Finally, in terms of the merger process, it is clear that, unlike class I flows, class II flows are dominated by dynamic vertical motions in the near-wall region. These motions are evidenced in the time-history sequence by the sharp salinity gradient regions which are pulled up along the wall and are subsequently folded back into the interior of the intrusions when they reach their apex. Although details of the initial merger process are not captured in the plots, a vivid example of the merger process can be seen in the three final frames of the time sequence for the two top intrusions. Here, vertical motions from the lower intrusion have penetrated into the intrusion above. A similar merger mechanism can be seen in photographs taken by Tanny and Tsinober [16]. From the salinity contour sequence, this merging process appears to be

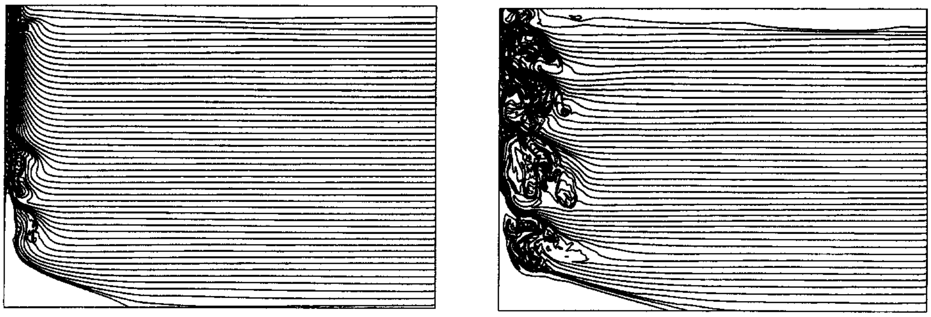

t = 4 minutes t = 8 minutes

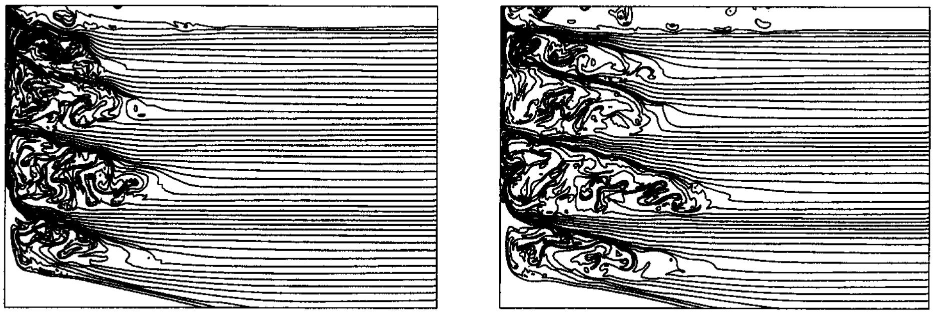

t = 12 minutes t = 16 minutes

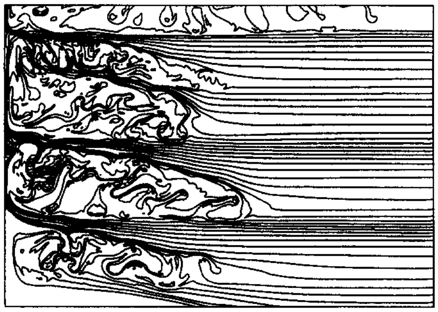

t = 20 minutes

Fig. 13. Salinity contours at various times of class II intrusions.

the result of an interface breakdown scenario rather than that of interface migration (both described by Linden [23]). In any case, this merging event is in contrast to the merger process observed in the previous section for class I intrusions, which was initiated by stronger intrusions blocking weaker ones from propagating and forcing them back to the heated wall. For both merger processes, fluid is eventually exchanged during merger; however, with class II flows the kinetic energy of the fluid in the near-wall region serves as the mechanism for merger.

5. CONCLUDING REMARKS

In this work, numerical simulations of two fundamentally different classes of convective intrusions, which develop due to the sidewall heating of a fluid with an initial linear two-component stratification, have been presented. Using a composite grid approach, it has been shown that an interface treatment based on local flux conservation cannot be employed. A revised interface treatment based on linear interpolation with conservative correction has been devised. The numerical results obtained for the two specific intrusion classes compare very favorably with the detailed experimental results presented by Schladow *et al.* [15] in terms of the physical characteristics of the intrusions, the internal salinity and temperature structures, the intrusion heights and the front propagation speeds. Most importantly, the fundamental differences in the merging processes of class I and II flows which were observed in the experiments

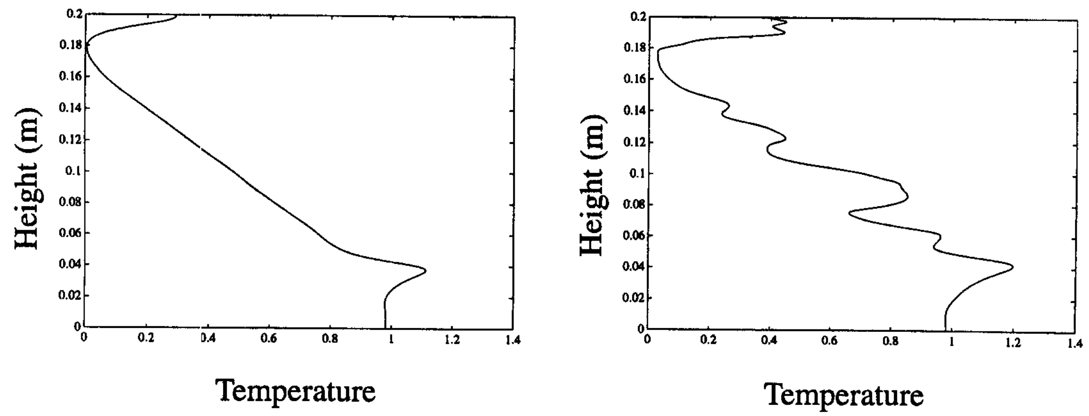

t = 4 minutes

t = 8 minutes

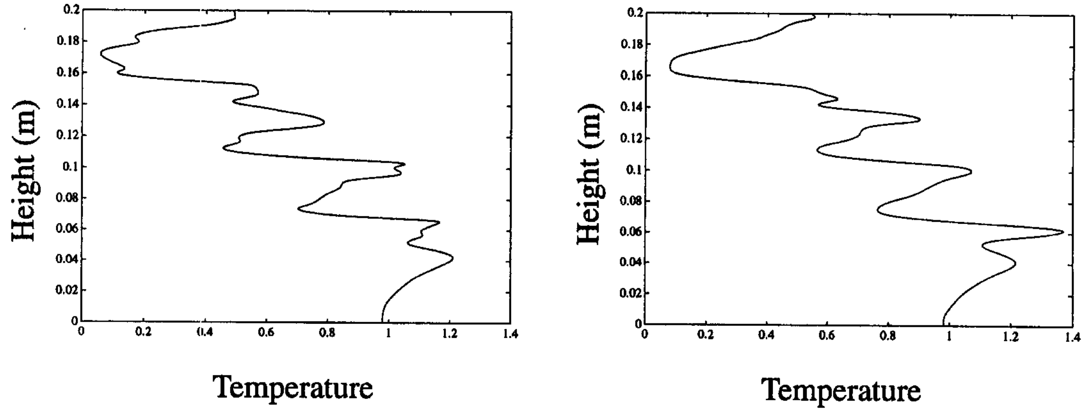

t = 12 minutes

t = 16 minutes

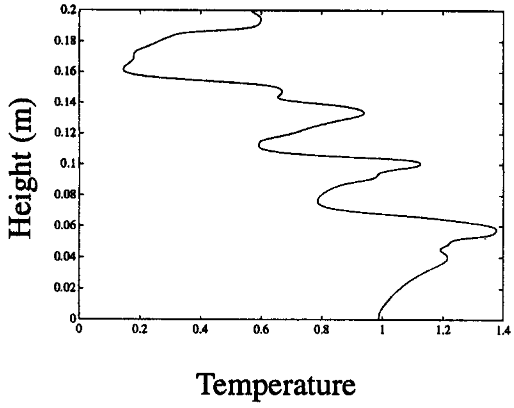

t = 20 minutes

Fig. 14. Temperature profiles at 3.0 cm from the heated wall at various times (class II).

have also been observed here. For class I intrusions, the numerical simulations clearly show the progressive weakening with time of intrusions due to the overtaking of neighboring intrusions above and below, which is consistent with the blockage mechanism described by Schladow *et al.* [15]. For class II intrusions, a breakdown of the interface separating neighboring intrusions is seen. This mechanism was also observed in the corresponding experimental results as well as in similar experiments performed by

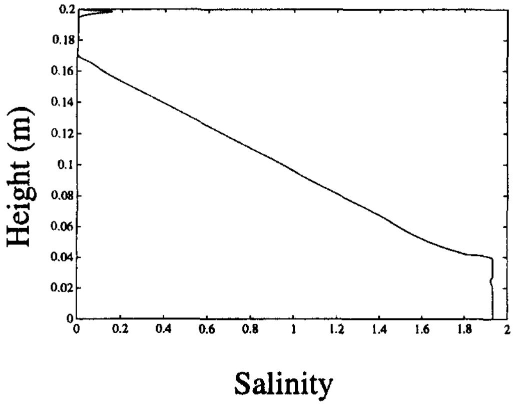

t = 4 minutes

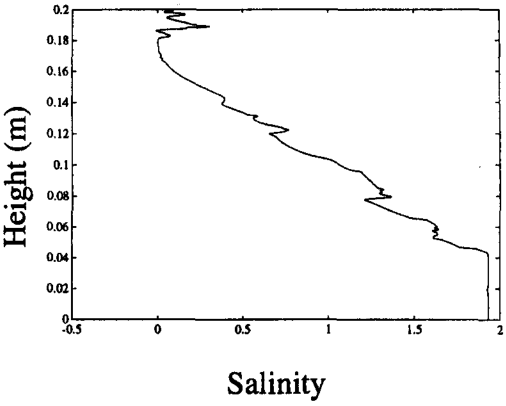

t = 8 minutes

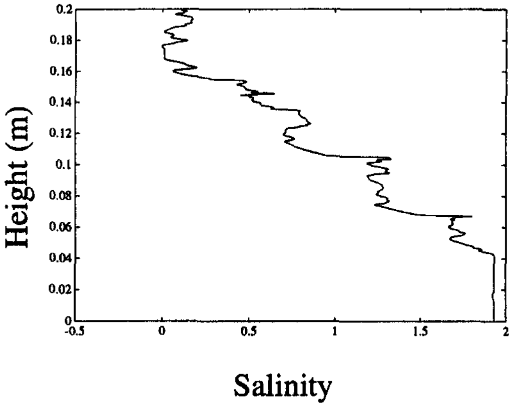

t = 12 minutes

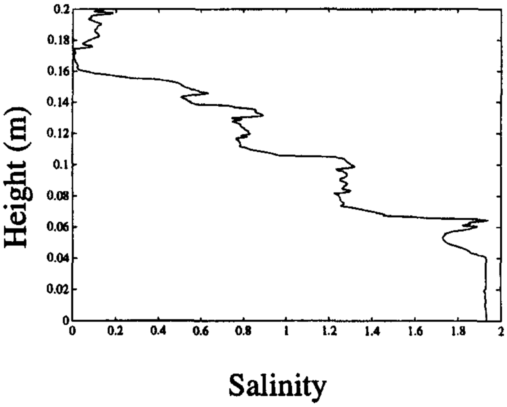

t = 16 minutes

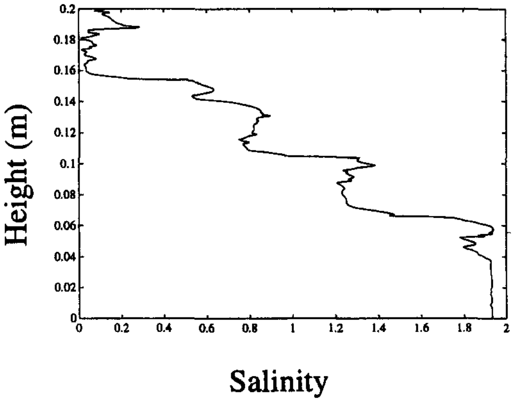

t = 20 minutes

Fig. 15. Salinity profiles at 3.0 cm from the heated wall at various times (class II).

Tanny and Tsinober [16]. In many instances, numerical simulations may provide insight into key physical mechanisms which may be difficult to obtain from the analysis of experimental data due to the various limitations of experimental equipment and procedures.

REFERENCES

1. T. L. Bergman and A. Ungan, Experimental and numerical investigation of double-diffusive convection induced by a discrete heat source, *Int. J. Heat Mass Transfer* **29,** 1695–1709 (1986).
2. K. Kamakura and H. Ozoe, Experimental and numerical analyses of double diffusive natural convection heated and cooled from opposing vertical walls with an initial condition of a vertically linear concentration gradient, *Int. J. Heat Mass Transfer* **36,** 2125–2134 (1993).
3. W. Shyy, *Computational Modelling for Fluid Flow and Interfacial Transport.* Elsevier, Amsterdam, The Netherlands (1994).
4. J. S. Turner, Double-diffusive phenomena, *A. Rev. Fluid Mech.* **6,** 37–57 (1974).
5. J. S. Turner, *Buoyancy Effects in Fluids.* Cambridge University Press, London (1979).
6. J. S. Turner, Multicomponent Convection, *A. Rev. Fluid Mech.* **17,** 11–44 (1985).
7. H. E. Huppert and J. S. Turner, Double-diffusive convection, *J. Fluid Mech.* **106,** 299–329 (1981).
8. R. A. Hoare, Problems of heat transfer in Lake Vanda, a density stratified antarctic lake, *Nature* **210,** 787–789 (1966).
9. H. E. Huppert and J. S. Turner, Ice blocks melting into a salinity gradient, *J. Fluid. Mech.* **100,** 367–384 (1980).
10. A. Akbarzadeh and P. Manins, Convective layers generated by side walls in solar ponds, *Solar Energy* **41,** 521–529 (1988).
11. B. S. Sherman and J. Imberger, Control of a solar pond, *Solar Energy* **46,** 71–81 (1991).
12. S. A. Thorpe, P. K. Hutt and R. Soulsby, The effect of horizontal gradients on thermohaline connection, *J. Fluid Mech.* **38,** 375–400 (1969).
13. C. F. Chen, D. G. Briggs and R. A. Wirtz, Stability of thermal convection in a salinity gradient due to lateral heating, *Int. J. Heat Mass Transfer* **14,** 57–65 (1971).
14. U. Narusawa and Y. Suzukawa, Experimental study of double-diffusive cellular convection due to a uniform lateral heat flux, *J. Fluid Mech.* **113,** 387–405 (1981).
15. S. G. Schladow, E. Thomas and J. R. Koseff, The dynamics of intrusions into a thermohaline stratification, *J. Fluid Mech.* **236,** 127–165 (1992).
16. J. Tanny and A. B. Tsinober, The dynamics and structure of double-diffusive layers in sidewall-heating experiments, *J. Fluid Mech.* **196,** 135–156 (1988).
17. R. A. Wirtz and L. H. Liu, Numerical experiments on the onset of layered convection in a narrow slot containing a stably stratified fluid, *Int. J. Heat Mass Transfer* **18,** 1299–1305 (1975).
18. J. C. Heinrich, A finite element model for double diffusive convection, *Int. J. numer. Methods Engng.* **20,** 465–477 (1984).
19. J. W. Lee and J. M. Hyun, Time-dependent double diffusion in a stably stratified fluid under lateral heating, *Int. J. Heat Mass Transfer* **34,** 2409–2421 (1991).
20. S. V. Patankar, *Numerical Heat Transfer and Fluid Flow.* Hemisphere, Washington DC (1980).
21. J. A. Wright and W. Shyy, a pressure-based composite grid method for the Navier–Stokes equations, *J. Comput. Phys.* **107,** 225–238 (1993).
22. M. M. Rai, A conservative treatment of zonal boundaries for euler equation calculations, *J. Comput. Phys.* **62,** 472–503 (1986).
23. P. F. Linden, The formation and destruction of finestructure by double diffusive process, *Deep-Sea Res.* **23,** 895–908 (1976).